Geophysical Journal International

Geophys. J. Int. (2013) **193,** 407–420 doi: 10.1093/gji/ggs123

An approach to improve Rayleigh-wave ellipticity estimates from seismic noise: application to the Los Angeles Basin

Toshiro Tanimoto, Tomoko Yano and Tomohiro Hakamata

Department of Earth Science and Earth Research Institute, University of California, Santa Barbara, CA 93106, USA. E-mail: toshiro@geol.ucsb.edu

Accepted 2012 December 21. Received 2012 September 25; in original form 2012 February 24

SUMMARY

We present an approach for seismic noise which improves Rayleigh-wave ellipticity estimates by reducing the influences from body waves and Love waves. The method requires three-component seismographs and uses the phase-shift information between the vertical and horizontal components. We select data that show the phase-shift of about 90° in order to separate Rayleigh waves from body waves and Love waves. In comparison to the usual H/V approach, the estimates for Rayleigh-wave ellipticity are systematically different by about 20 per cent because the existence of *S* waves and Love waves systematically increases horizontal amplitudes. The differences in the inverted *S*-wave velocity structure reach up to about 20 per cent in the upper 20 km. The method is limited to a relatively low-frequency range, below 0.3 Hz, as the 90° phase-shift peaks become difficult to identify above 0.3 Hz. Despite this limitation in the frequency range, this approach can improve the *S*-wave velocity structure in the upper 5–10 km, which should lead to a better prediction of long-period ground motions for periods of about 5–10 s. An improved prediction of such long-period ground motion is important for hazard mitigation in the world's metropolitan areas with high-rise buildings. This approach is applied to the structure in the broader Los Angeles basin in Southern California and improvement of the reference velocity structure in the upper 5–10 km is demonstrated.

Key words: Earthquake ground motions; Site effects; Wave propagation.

1 INTRODUCTION

Many urban areas in the world are often in regions of thick sedimentary layers because they tend to have developed in large river deltas or close to lake beds. If such an area is in a high seismicity region, seismic hazard mitigation becomes a high-priority issue for the region because amplification of seismic waves in a thick sedimentary region may be quite significant. The depth distribution of *S*-wave velocities is the key parameter for this amplification effect.

Both the active-source and passive-source methods have been developed for the retrieval of shallow *S*-wave velocity structure in the last 30 yr (for review, Boore 2006). The passive-source approaches have gained considerable attention in recent past, as the quality and density of seismic stations have improved systematically and seismic noise is always available.

The passive-source methods can be classified into three different kinds; (i) the frequency-wavenumber method (e.g. Horike 1985; Tokimatsu 1997; Kawase *et al.* 1998; Liu *et al.* 2000), (ii) the SPAC method (Aki 1957; for review, Okada 2003) and the related noise cross-correlation method (Campillo & Paul 2003; Shapiro *et al.* 2005) and (iii) the H/V method (Nakamura 1989; Bard 1998; Konno & Ohmachi 1998; Scherbaum *et al.* 2003). This paper is related to the third (H/V) method and proposes an improvement in the low-frequency band (below 0.3 Hz).

The H/V method has been one of the most popular approaches, because it is basically a single-station method, requiring only three-component seismographs. It has a long history in Japan (e.g. Nogoshi & Igarashi 1971; Nakamura 1989; Yamanaka *et al.* 1994; Tokimatsu 1997; Arai & Tokimatsu 2004), in Europe (e.g. Bard 1998; Scherbaum *et al.* 2003; Fäh *et al.* 2003; Parolai *et al.* 2005, 2006), and in US (e.g. Asten & Boore 2005). The list of papers is literally exploding, as the approach is being applied constantly to new regions.

The interpretation of the *H*/*V* ratios remains a problematic issue, however. The peaks in the *H*/*V* ratios were initially interpreted as body-wave resonance (Nakamura 1989), and indeed some later studies supported this contention by showing resonance of *SH* waves near the surface (e.g. Field & Jacob 1993; Lermo & Chavez-Garcia 1994; Fah *et al.* 2001; Bonnefoy-Claudet *et al.* 2006). But the interpretation of the *H*/*V* ratio as Rayleigh-wave ellipticity also became popular (e.g. Lachet & Bard 1994; Yamanaka *et al.* 1994; Kudo 1995; Bard 1998; Konno & Ohmachi 1998) and the controversy basically continues until today.

On this issue, we need to pay attention to two aspects of the problem. First, considerations for frequency range are crucially important, as the mechanisms of noise excitation may differ from frequency to frequency. Many studies reported results in the frequency band 0.5–10 Hz, but some included data from 0.1 Hz and others extended the high-frequency end to 20–30 Hz (Boore 2006). Excitation sources of seismic noise may differ for such a wide frequency band. For example, seismic noise below 0.5 Hz, especially about 0.05–0.3 Hz, is predominantly excited by ocean waves. The existence of primary (about 0.07 Hz) and secondary peaks in noise (about 0.15 Hz) matches the prediction of the Longuet-Higgins' mechanism for ocean waves (Longuet-Higgins 1950) and supports that such low-frequency noise is excited by ocean waves. Observational studies in this frequency range often showed spatially concentrated sources (Cessaro 1994; Friedrich *et al.* 1998; Schulte-Pelkum *et al.* 2004). On the other hand, high-frequency noise above 1 Hz often shows contrast between day and night (based on local time) and indicates that much of the energy is of cultural origin. Spatial distribution of excitation sources is more likely to be widespread. These differences in excitation mechanisms can lead to great differences in the ratios of excited seismic waves among *S* waves, Rayleigh waves and Love waves.

Second, any type of excitation sources generally excites all types of seismic waves. The Longuet-Higgins' mechanism, for example, is basically a vertical force in the ocean and it is an efficient excitation source for Rayleigh waves, but it should also generate body waves. If the sea floor is oblique or has topography, it can excite Love waves. Also, the interactions between ocean waves and seafloor topography should result in equivalent horizontal forcing (Saito 2010), and they should excite Love waves in addition to body waves and Rayleigh waves. Furthermore, if there exists a sharp lateral boundary, Rayleigh waves may convert to Love waves. Therefore, seismic noise must generally contain all kinds of waves, and the question is on relative amplitudes among body waves, Love waves and Rayleigh waves, rather than which type of waves explain the *H*/*V* ratios (Bonnefoy-Claudel *et al.* 2008).

Recent theoretical efforts by Lunedei & Albarello (2010) and Sanchez-Sesma *et al.* (2011) accept this situation and attempt to analyse the *H*/*V* data as consisting of various types of waves. It is a promising approach, although it must be noted that such studies make assumptions about temporal and spatial characteristics of the excitation sources that are basically unknown.

In this paper, we adopt an alternative, observational approach to produce a Rayleigh-wave dominated data set. This will lead to an improved estimate for Rayleigh-wave ellipticity because it can reduce a large fraction of body waves and Love waves from data. We can then invert the measured Rayleigh-wave ellipticity for *S*-wave structure. Our approach is limited to a narrow low-frequency band, 0.1–0.3 Hz, because the technique is difficult to apply above 0.3 Hz. However, despite this limitation, the data in this frequency range can contribute to understanding *S*-wave velocity structure in the upper 5–10 km of the crust. Improving the structure in this depth range will be important for prediction of long-period ground motion about 5–10 s. Seismic hazard mitigation in such a long-period range is becoming important for metropolitan areas with high-rise buildings, as demonstrated by the long shaking of high-rise buildings not only in Tokyo, but also in Osaka (which is more than 500 km away) by the 2011 Tohoku-Oki, $M = 9.0$, earthquake.

In this paper, we discuss our results in the following order. We first demonstrate our technique which enables isolation of Rayleigh waves using phase-shift information (Section 2). We then discuss the resulting differences in Rayleigh-wave ellipticity measurements and the effects they make on the *S*-wave velocity structure. We then apply the technique to stations in the broader Los Angeles metropolitan area (Section 3). We discuss regional characteristics in the Rayleigh-wave ellipticity values and the *S*-wave velocity structure in the upper 10 km that can be derived.

2 APPROACH

The broadband seismic data from about 150 stations in Southern California are available from the Southern California Earthquake Center (SCEC) data centre. In this study, we used a subset of this network whose locations are shown in Fig. 1.

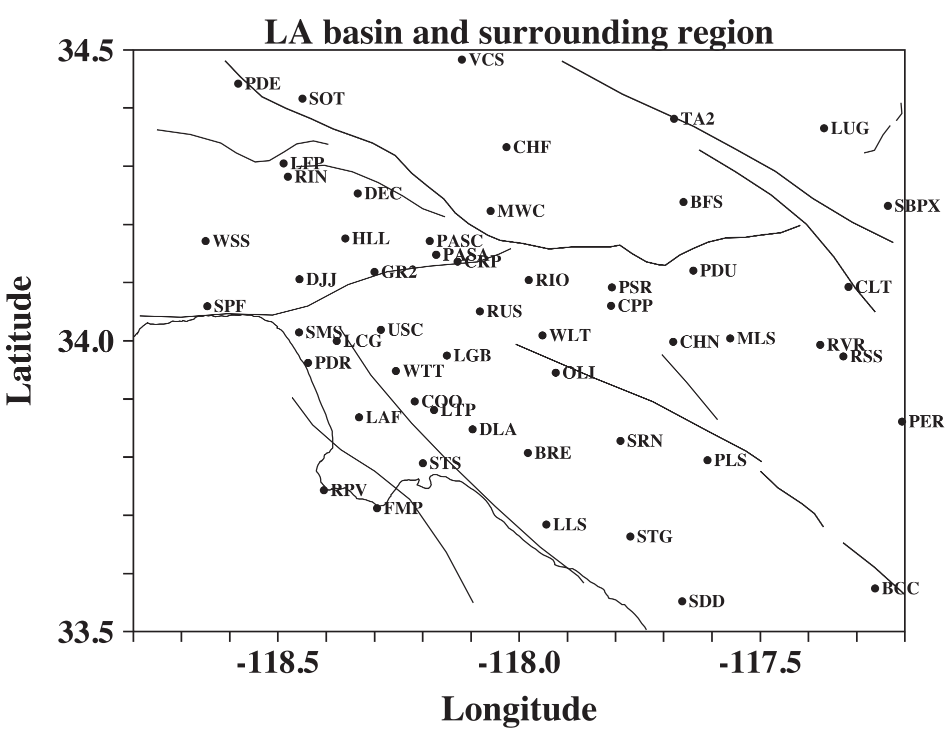

Figure 1. Location of broadband seismic stations used in this study.

We will first describe the key information in our approach, the phase-shift data between the vertical and horizontal components in (2.1) which enables us to isolate Rayleigh-wave energy from other types of waves. We then discuss the impact on the estimates for Rayleigh-wave ellipticity (2.2) and the resultant differences in the *S*-wave velocity structure (2.3).

2.1 Retrieval of Rayleigh-wave ellipticity

First, let us define our notation. Fourier spectra for the three components are given by

$$\mathbf{Z}(\omega) = \int_{T_0}^{T_1} u_z(t)\, e^{-i\omega t}\, \mathrm{d}t,$$

$$\mathbf{N}(\omega) = \int_{T_0}^{T_1} u_n(t)\, e^{-i\omega t}\, \mathrm{d}t,$$

$$\mathbf{E}(\omega) = \int_{T_0}^{T_1} u_e(t)\, e^{-i\omega t}\, \mathrm{d}t, \tag{1}$$

where $u_z(t)$, $u_n(t)$ and $u_e(t)$ are three-component seismograms for the vertical, the north–south and the east–west components, $T_1 - T_0$ is the length of time series (1 hr in this study) and $\mathbf{Z}(\omega)$, $\mathbf{N}(\omega)$ and $\mathbf{E}(\omega)$ are the complex Fourier spectra at an angular frequency ω.

We analysed continuous data for stations in Fig. 1 for the years 2002 and 2003. We computed Fourier spectra for every 1-hr record over 2 yr. We then determined the azimuth ϕ of the maximum horizontal amplitude for each 1-hr record by maximizing the quantity I:

$$I = \sum_{i=1}^{n} |\mathbf{N}(\omega_i)\cos\phi + \mathbf{E}(\omega_i)\sin\phi|^2. \tag{2}$$

For each frequency $f\,(=\omega/2\pi)$, we searched for the maximum by examining this quantity at an interval of 0.1°. The upper limit of this summation, n, is the number of discrete frequencies within the frequency range $f \pm 0.01$ Hz. For example, for 0.15 Hz, we used a narrow frequency range between 0.14 and 0.16 Hz. The inclusion of adjacent frequencies stabilized the results for the determination of the maximum amplitude, while determination from a single frequency data led to larger scatter in results (Tanimoto *et al.* 2006).

If the data were gapless and contain good signals over 2 yr, we can get 17 520 one-hour time windows. However, since we apply two criteria in order to filter out non-Rayleigh-wave signals, this number typically became about $n = 3000$. Here, good signals mean fairly constant estimates of ZH in the absence of earthquakes, which is defined below by eq. (3).

Once we determined the azimuth, ϕ, of the maximum horizontal amplitude, we computed the amplitude in that direction (hereafter referred to as H) and the amplitude in the perpendicular direction (referred to as T). We compute the ratio between the vertical and horizontal amplitudes by

$$ZH = \frac{Z(f)}{H(f)}, \tag{3}$$

which is the inverse of the H/V ratio. This should be equivalent to analysing the H/V ratio in principle, but we prefer to use the ratio in (3) for the frequency band 0.1–0.3 Hz because the vertical amplitudes could disappear for a basin structure in this frequency band (Konno & Ohmachi 1998; Tanimoto & Rivera 2005). Use of (3) is simply to avoid a situation, akin to division by zero. Hereafter, we refer to this ratio as Rayleigh-wave ellipticity.

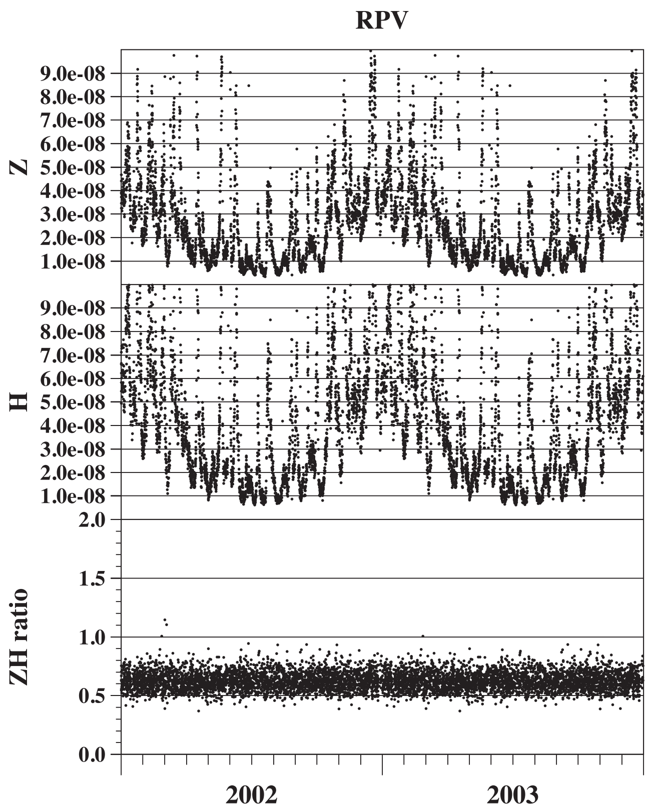

Figure 2. Variations of spectral amplitudes at 0.15 Hz over 2 yr. They were computed for every 1 hr record (time series). From top to bottom, they are for vertical (Z) and maximum horizontal displacement (H) and the ratio between them. Seasonal changes are obvious for Z and H, but their ratios are constant throughout the years (2002–2003). The station is RPV.

Fig. 2 shows the vertical amplitude (Z), the horizontal amplitudes (H) and their ratios (ZH) for station Rancho Palos Verdes (RPV) from every 1-hr record. The results are for a frequency of 0.15 Hz. The results in Fig. 2 do not contain ratios from all 1-hr records, as we apply two additional criteria to reduce effects from body waves and Love waves.

The first is the selection of data based on phase-shift between the vertical and horizontal amplitudes. Fig. 3 shows histograms for four stations at 0.15 Hz. The number of 1-hr records was computed for each phase-shift bin (10° bin). The abscissa is the phase-shift angle, derived from the phase-shift between $Z(f)$ and $H(f)$, and the ordinate is the number of data for each bin. There are some variations among different seismic stations but the maximum number of data typically appears near the phase-shift angle of 90°. We interpret that the data near this maximum are dominated by Rayleigh waves, since body waves would have no phase-shift between the vertical and horizontal components and Love waves do not have vertical amplitudes.

The second criterion is on the ratio of amplitudes H/T. We removed records that have this ratio less than 3.0. This procedure is aimed at removing Love-wave signals as this ratio H/T is similar to the radial to transverse amplitudes.

Note that the vertical and horizontal amplitudes in Fig. 2 vary about a factor of 10 from season to season, while the ratios between them stay nearly constant as shown in the bottom panel. The most natural explanation for this constancy is that those ratios are controlled by Rayleigh waves, as the ellipticity of Rayleigh-wave particle motion at a location is determined by the local structure (or the shape of an eigenfunction for the local structure).

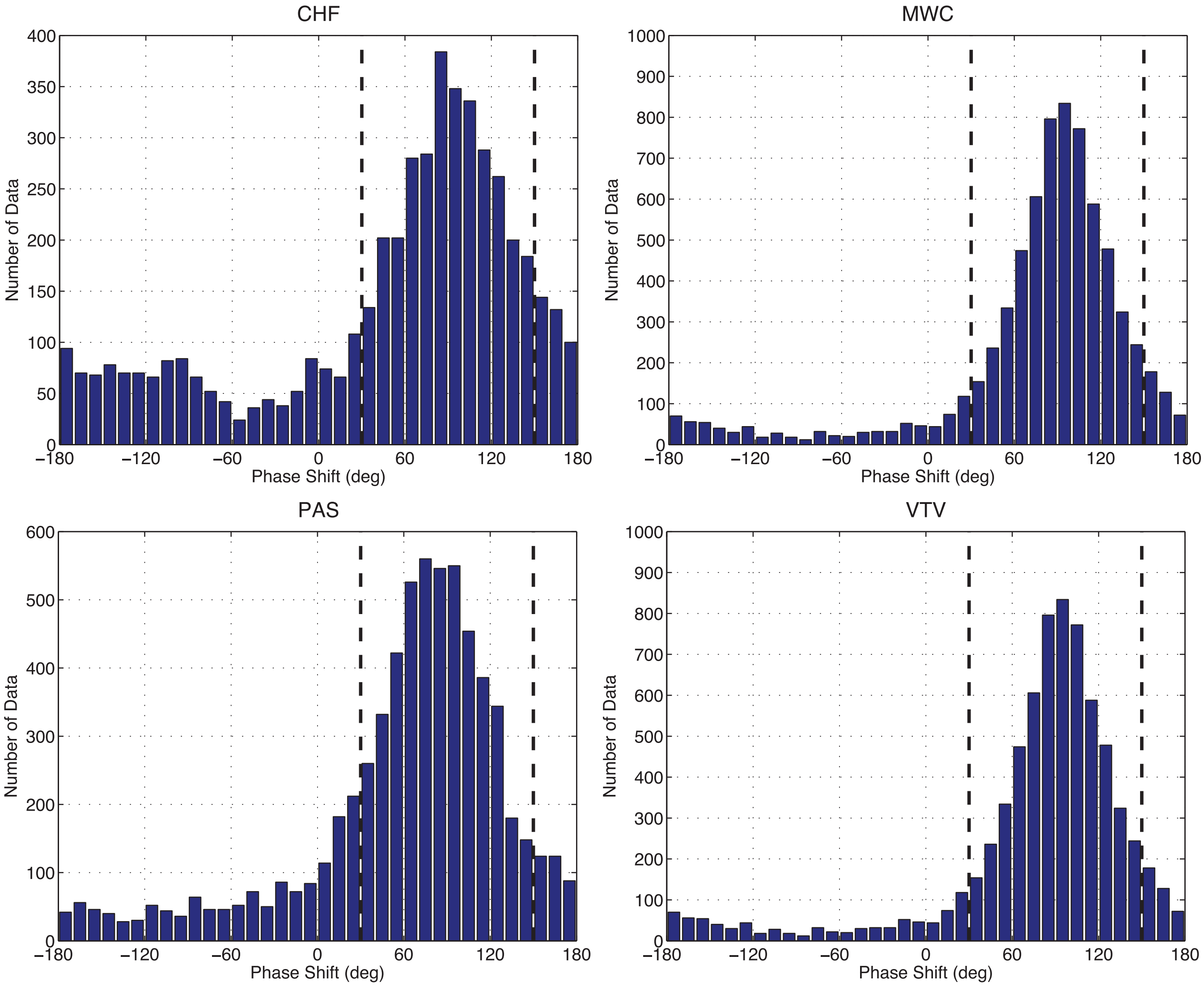

Figure 3. Histograms of phase-shift angles between the vertical and horizontal components. Results for four stations (CHF, MWC, PAS and VTV) are shown. The abscissa is the phase-shift between vertical and horizontal components, and the ordinate is the number of 1 hr time series for each station in 2002 and 2003. The peaks near 90° indicate that there are Rayleigh waves in these data. Two dash lines indicate 30° and 150°. Rayleigh-wave ellipticity were derived by using data between these angles. Values for different ranges are shown in Tables 1 and 2.

2.2 Comparison to previous approach: effects of Love waves

In the usual *H*/*V* approach, the ratios are calculated from Fourier amplitudes without any selection of data. If Love waves make up a significant portion of data, it would enhance horizontal amplitudes systematically and introduce bias in the estimates of Rayleigh-wave ellipticity. This is a concern. Love-wave energy may be comparable to Rayleigh-wave energy, as some studies showed comparable energy in the microseismic frequency band between 0.05 and 0.3 Hz (e.g. Capon 1972; Nishida *et al.* 2008).

If we were to measure the ratios without applying our selection criteria, the ratios should be given by

$$ZH = \sqrt{\frac{|Z(f)|^2}{|H_R(f)|^2 + |H_T(f)|^2}}, \tag{4}$$

where we denote horizontal spectra for Rayleigh waves by H_R and those for Love waves and *S* waves by H_T. Depending on the size of $|H_T(f)|$, the measured ratios can deviate from Rayleigh-wave ellipticity. Our approach basically attempts to minimize this term using the phase-shift information.

Table 1 shows the *ZH* computed for different phase-shift intervals for the seismic station GLA. Frequency range is from 0.1 to 0.3 Hz. The second to the fourth columns are the results for the phase-shift angle range of 60°–120°, 45°–135°and 30°–150°, all centred about 90°. Dashed lines in Fig. 3 indicate 30° and 150°. We estimated Rayleigh-wave ellipticity using data from these bounds that bracket the 90°. The fifth column (ALL) shows the ratios computed for all phase-shift angles, thus including Love waves and *S* waves in horizontal amplitudes. The uncertainties (1σ) for this case (ALL) are shown in the sixth column. They are about 0.1. The uncertainties for the first three columns are smaller but are of the same order.

The variations in Rayleigh-wave ellipticity among the first three cases in Table 1 (phase shift ranges 60°–120°, 45°–135° and 30°–150°) are small, considering the size of uncertainties. But the differences between these cases and the fifth column (ALL) are significant and reach 26 per cent. Within the frequency range 0.1–0.3 Hz, the

Table 1. Station GLA. Comparison of Rayleigh-wave ellipticity values derived for different phase-shift ranges (Fig. 3). ALL includes all angles and is affected by body waves and Love waves. The sixth column is the 1σ error for ALL (the fifth column).

Freq (Hz)	60–120	45–135	30–150	ALL	Error (ALL)
0.100	1.077	1.060	1.050	0.797	0.154
0.110	1.096	1.091	1.083	0.867	0.112
0.120	1.108	1.106	1.105	0.888	0.087
0.130	1.092	1.091	1.091	0.886	0.079
0.140	1.121	1.120	1.121	0.912	0.080
0.150	1.139	1.138	1.137	0.912	0.082
0.160	1.086	1.083	1.082	0.854	0.081
0.170	1.010	1.012	1.007	0.802	0.081
0.180	0.987	0.990	0.992	0.790	0.084
0.190	1.030	1.031	1.030	0.829	0.096
0.200	1.088	1.093	1.096	0.901	0.117
0.210	1.142	1.144	1.154	0.981	0.134
0.220	1.159	1.159	1.160	0.989	0.133
0.230	1.141	1.143	1.150	0.955	0.121
0.240	1.128	1.128	1.131	0.926	0.109
0.250	1.121	1.125	1.130	0.905	0.100
0.260	1.109	1.111	1.116	0.900	0.097
0.270	1.071	1.075	1.077	0.869	0.093
0.280	1.046	1.053	1.054	0.844	0.093
0.290	1.050	1.049	1.053	0.844	0.095
0.300	1.050	1.053	1.056	0.840	0.095

Table 2. Same with Table 1 except that this table is for station PAS.

Freq (Hz)	60–120	45–135	30–150	ALL	Error (ALL)
0.100	0.935	0.925	0.923	0.744	0.106
0.110	0.944	0.944	0.945	0.780	0.087
0.120	0.914	0.914	0.915	0.773	0.076
0.130	0.907	0.906	0.905	0.756	0.071
0.140	0.904	0.908	0.907	0.748	0.069
0.150	0.962	0.965	0.964	0.798	0.077
0.160	1.077	1.074	1.072	0.881	0.087
0.170	1.109	1.112	1.113	0.893	0.086
0.180	1.115	1.115	1.113	0.881	0.083
0.190	1.080	1.084	1.087	0.873	0.091
0.200	1.058	1.059	1.061	0.859	0.096
0.210	1.069	1.072	1.073	0.868	0.098
0.220	1.075	1.081	1.088	0.877	0.099
0.230	1.117	1.111	1.109	0.896	0.104
0.240	1.114	1.112	1.114	0.903	0.105
0.250	1.110	1.104	1.106	0.890	0.102
0.260	1.049	1.051	1.056	0.847	0.093
0.270	0.975	0.978	0.980	0.781	0.084
0.280	0.965	0.958	0.962	0.769	0.084
0.290	0.974	0.982	0.974	0.779	0.085
0.300	0.971	0.964	0.965	0.770	0.083

differences vary from 16 to 26 per cent. These differences are most likely caused by the effects of $H_T(f)$ in the above formula.

Tables 2 and 3 show the results for stations PAS and CHF, respectively. In both cases, the differences among the first three cases (phase shift 60°–120°, 45°–135° and 30°–150°) are small and the results for all phase shifts (between -180° and 180°) are systematically smaller. In the case of PAS (Table 2), the differences vary from 15 to 21 per cent. In the case of CHF (Table 3), the differences vary between 10 and 28 per cent for frequencies 0.1–0.3 Hz. We also applied similar analyses to other stations and confirmed that most stations show typically 20 per cent changes for the estimates of Rayleigh-wave ellipticity.

Table 3. Same with Table 1 except that this table is for station CHF.

Freq (Hz)	60–120	45–135	30–150	ALL	Error (ALL)
0.100	0.898	0.885	0.875	0.804	0.117
0.110	0.952	0.944	0.934	0.815	0.111
0.120	0.965	0.958	0.952	0.816	0.106
0.130	0.906	0.903	0.900	0.832	0.105
0.140	0.907	0.899	0.895	0.857	0.111
0.150	0.969	0.966	0.963	0.840	0.110
0.160	0.990	0.987	0.985	0.778	0.100
0.170	0.988	0.985	0.983	0.760	0.096
0.180	1.011	1.007	1.005	0.820	0.109
0.190	1.049	1.045	1.041	0.838	0.113
0.200	1.031	1.031	1.031	0.783	0.104
0.210	0.962	0.963	0.963	0.764	0.103
0.220	0.946	0.943	0.940	0.760	0.102
0.230	0.989	0.989	0.989	0.751	0.102
0.240	1.027	1.026	1.026	0.744	0.100
0.250	0.954	0.958	0.959	0.753	0.102
0.260	0.922	0.930	0.935	0.779	0.108
0.270	0.914	0.916	0.917	0.785	0.108
0.280	0.917	0.921	0.923	0.777	0.107
0.290	0.895	0.894	0.894	0.762	0.106
0.300	0.894	0.896	0.897	0.749	0.104

These differences in ellipticity estimates provide us some information on the relative size of Love-wave energy to Rayleigh-wave energy. If Love-wave energy and Rayleigh-wave energy were comparable, Rayleigh-wave ellipticity estimates by eq. (3) were biased by $1/\sqrt{2} \approx 0.71$, which is about 30 per cent. Since our analysis indicates about 20 per cent change rather than 30 per cent, it indicates that Rayleigh wave energy is more than Love wave energy.

If we take the case of GLA (Table 1), the ratio between our approach and the case for ALL (including Love waves) is about 1.25. Assuming that our approach yields the value with $H_T(f) \approx 0$ in the above formula, we get an estimate $|H_T/H_R|^2 = 0.56$. This result suggests that Love-wave energy (which may include some *S* waves) is about half of Rayleigh wave energy. From station to station, this energy ratio differs but remains in the range of 40–70 per cent.

2.3 Effects on *S*-wave velocity structure

In Section 2.2, we pointed out that our Rayleigh-wave ellipticity estimates were different about 20 per cent from the usual *H*/*V*-type approach. In this section, we examine the effects on *S*-wave velocity structure that are caused by these differences.

We inverted these Rayleigh-wave ellipticity data for the *S*-wave velocity structure by using an iterative nonlinear inversion. For the inversion of the *H*/*V* data, many other approaches are available. One of the significant approaches is by Yamanaka & Ishida (1996), which used the genetic algorithm to make a thorough search for the global minimum. It has been adopted by many studies since then (e.g. Parolai *et al.* 2005). This approach is quite powerful in that it can explore a wide range of parameter space in search of the global minimum.

We do not use this approach in our study, however, because there already exists well-established reference models for Southern California. The Southern California Earthquake Center has developed the community velocity models (SCEC CVM; Kohler *et al.* 2003; Plesch *et al.* 2009) in the last 20 yr that incorporate results from the crustal tomographic results (Hauksson 2000), the mantle tomographic results (Prindle & Tanimoto 2006) and near-surface corrections that are based on VS30, sonic log and industry reflection data (Süss & Shaw 2003). It is currently going through the updates by the adjoint-inversion approaches that incorporate 3-D numerical simulations (Chen *et al.* 2007; Tape *et al.* 2009, 2010). Since the models satisfy many different types of seismological data already, it is most constructive to incorporate our results through the perturbations of available SCEC CVM models, rather than attempting to find a completely different structure that may be associated with a local minimum of this nonlinear inverse problem.

In this study, we used the model SCEC CVM-H 6.2 (Plesch *et al.* 2009) for the starting model. This is not the most recent model but was adopted as a demonstration of our approach. At the same time, as far as the average structure in the upper 10 km is concerned, it does not differ much from newer models.

Let us denote the Rayleigh-wave ellipticity by ϵ and its perturbation by $\delta\epsilon$. Then, we can write the relation between $\delta\epsilon/\epsilon$ and perturbations in density, P-wave velocity and S-wave velocity by

$$\frac{\delta\epsilon}{\epsilon} = \int_0^R \left\{ K_\rho(r)\frac{\delta\rho}{\rho} + K_\alpha(r)\frac{\delta\alpha}{\alpha} + K_\beta(r)\frac{\delta\beta}{\beta} \right\} \mathrm{d}r, \tag{5}$$

where R is the radius of the Earth and the three kernels K_ρ, K_α and K_β are the depth sensitivity kernels for density (ρ), P-wave velocity (α) and S-wave velocity (β). Their perturbations are written by $\delta\rho$, $\delta\alpha$ and $\delta\beta$, respectively.

For the computations of these kernels, K_ρ, K_α and K_β, we use our own software based on the variational principle for the Rayleigh-wave ellipticity, derived in Tanimoto & Tsuboi (2009). Fig. 4 shows the depth sensitivity kernels for the average Southern California structure. The left columns are K_ρ (red), K_α (green) and K_β (blue) for 0.1 and 0.2 Hz.

Since there are three independent parameters, we could form other parameters for the depth inversion. If we were to take ρ, α and β/α (the ratio of S-wave velocity to P-wave velocity) as the three parameters, we would get the kernels in the middle panels (top panel 0.1 Hz, bottom panel 0.2 Hz) and if we were to take ρ, α and ν (Poisson's ratio) as three parameters, we get the results in the right panels. We found no particular advantage for a particular choice of these schemes. We simply adopted the left case for the inversion of seismic structure. It might be useful to note that all three cases indicate that Rayleigh wave at 0.10 Hz is sensitive to the average structure in the top 10 km of the Earth and those at 0.20 Hz are sensitive to the structure in the top 5 km.

Among the three parameters (density, P-wave velocity and S-wave velocity), Rayleigh-wave ellipticity data are most sensitive to S-wave velocity structure. However, the sensitivity to P waves is not necessarily small at shallow depths. Therefore, we introduced a relation $\delta\alpha/\alpha = 0.75\delta\beta/\beta$ to take its effects into account. This choice was made through examinations of a range of parameters in our previous study (Tanimoto & Alvizuri 2006). A different choice of the coefficient, say 0.5 instead of 0.75, modifies the results to some extent but the overall features of velocity structure are not affected (Yano *et al.* 2009). Effects from the density structure are not included in this study.

Examples of the iterative-inversion results for seismic structure beneath four stations (CHF, MWC, PAS and VTV) are shown in Figs 5(a) and (b). For each station, the Rayleigh-wave ellipticity data are shown in the top panels. The observed ellipticity data by our approach are shown by blue with 1σ error bars and those without our two criteria are shown by red with 1σ error bars. The frequency range is from 0.1 to 0.3 Hz. Black dashed lines in the top panels are the theoretical Rayleigh-wave ellipticity for the starting structure. Mismatches between these theoretical values and the measured values are quite large and indicate that S-wave velocity structure must have significant perturbations to satisfy the Rayleigh-wave ellipticity data.

We typically iterated 40 times to get to the final velocity models. Fit to the data are shown by blue lines and red dash lines in the top panels of Figs 5(a) and (b). The corresponding S-wave velocity models are shown in the bottom panels for each case. The inverted S-wave structures for our measurements are shown by solid blue lines and those for the measurements without our criteria (possibly containing strong influence from Love waves) are shown by red dash.

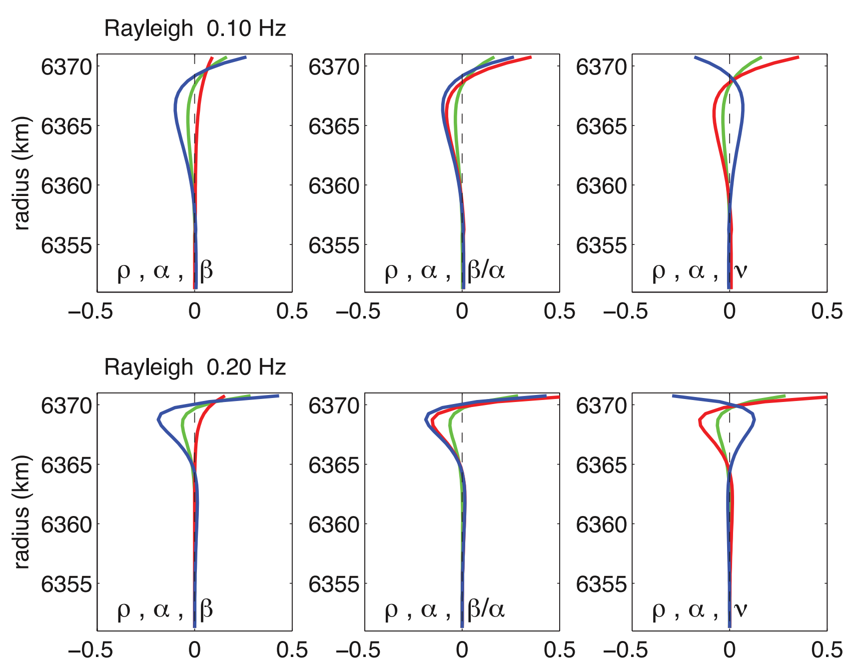

Figure 4. Depth sensitivity kernels for the Rayleigh-wave ellipticity at 0.10 Hz (top) and at 0.20 Hz (bottom). In the left panel, the kernel for density is green, the kernel for P waves is red and the kernel for S waves is blue. In the right panel, boundary perturbations are shown, but they were not used in this study.

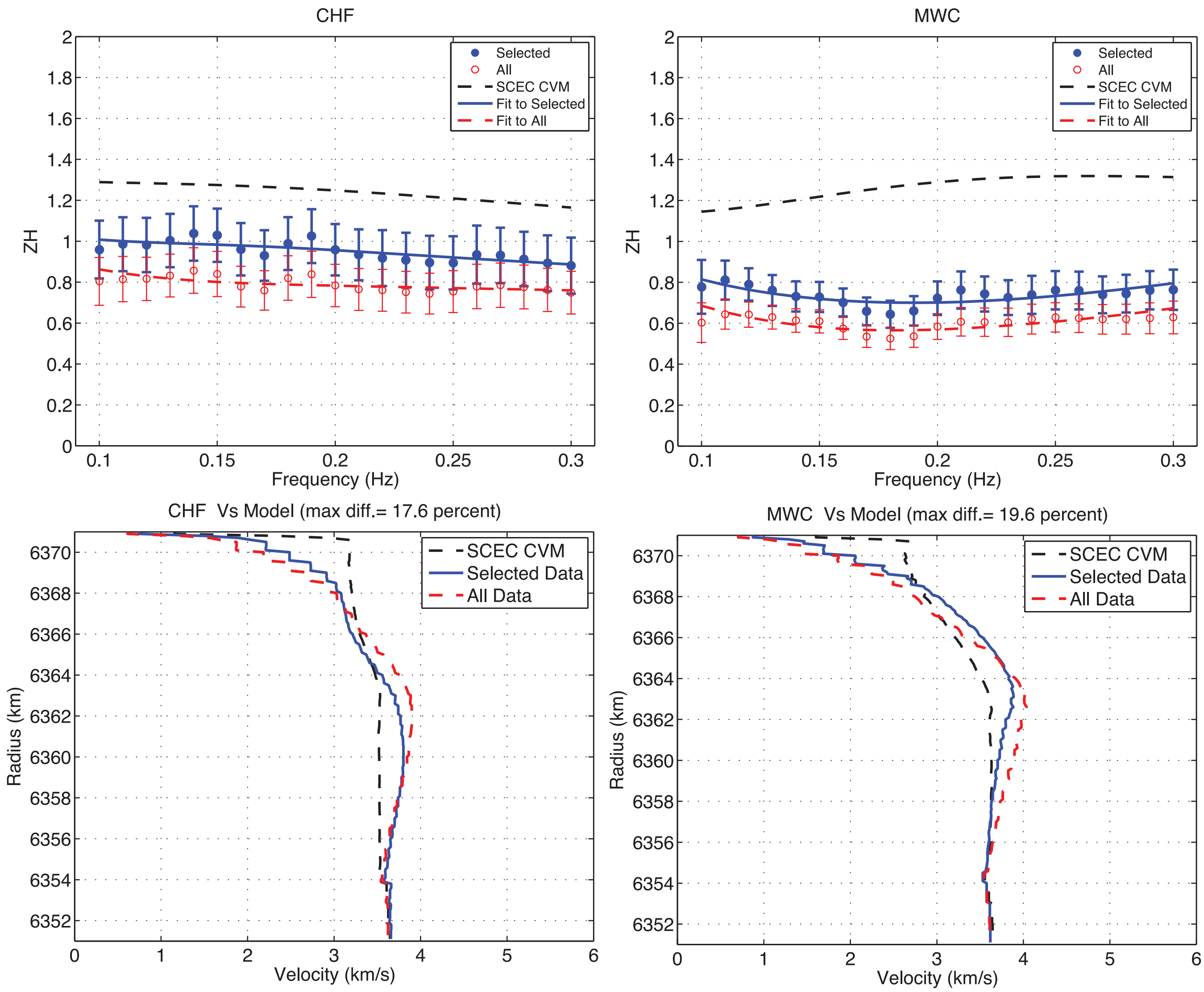

Figure 5. (a) (Top) Goodness of fit to the Rayleigh-wave ellipticity data at CHF (left) and MWC (right). The estimates by our approach are shown in blue and those without our two criteria, which do not filter out non-Rayleigh-wave energy, are shown in red. Theoretical values for the starting model (SCEC CVM 6.2) are shown by black dashes. Fit to data by the final models are shown by blue solid line and red solid line. (Bottom) The corresponding *S*-wave velocity distribution with depth. The starting model is shown in black dash. Differences between blue and red reaches 17.6 per cent for CHF (left) and 19.6 per cent for MWC. These are the maximum differences in *S*-wave velocity in the top 20 km. (b) Same with Fig. 5(a) except that these are for stations PAS and VTV. The maximum *S*-wave differences are 22.9 per cent (PAS) and 11.5 per cent for VTV. VTV shows one of the smallest differences in the *S*-wave velocity structure.

Resulting differences in the *S*-wave velocity models are typically 20 per cent, similar to the differences in the Rayleigh-wave ellipticity values. But the differences in *S*-wave velocity structure vary with depth. The perturbations often change their sign over the 20-km depth range, which means the differences are smaller for some depth ranges. The maximum *S*-wave velocity differences are given in each panel (in the title), varying from 11.5 per cent (VTV) to 22.9 per cent (PAS).

3 LOS ANGELES BASIN AREA

3.1 Basin signature

We applied our technique to stations in Fig. 1. Rayleigh-wave ellipticity was measured from 0.13 to 0.30 Hz for all stations. For the stations in Figs 5(a) and (b), we used the lowest frequency of 0.10 Hz, but some other stations in Fig. 1 did not yield good measurements below 0.13 Hz. In order to maintain consistency among stations, specifically for obtaining balanced spatial resolution, we adopted 0.13 Hz as the lowest frequency limit for the results in this section.

There is a characteristic pattern in the Rayleigh-wave ellipticity values in the basin. In order to show this feature, four examples from each region, inside and outside the basin, are shown in Figs 6(a) and (b). The main difference between these groups is that the ellipticity values in the basin (Fig. 6b) show a minimum around 0.13–0.16 Hz, whereas those outside the basin generally show nearly constant values (often close to the value 1).

Small ellipticity values mean that Rayleigh-wave particle motions are horizontally elongated, such as those seen near the frequency 0.15 Hz in the basin. This feature becomes less evident towards higher frequencies and almost disappears above 0.25 Hz. The ellipticity values do not show much geographic variations above 0.25 Hz.

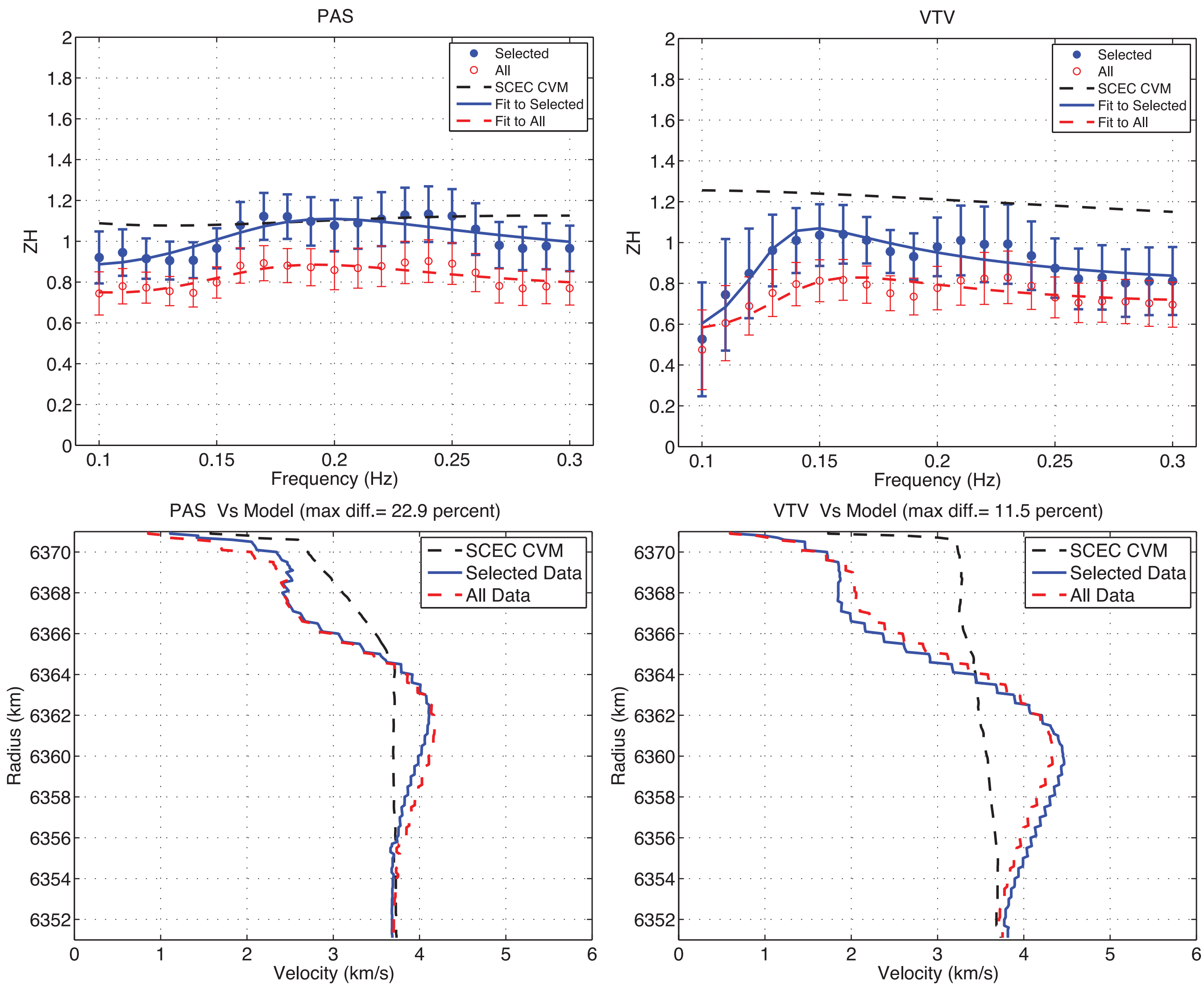

Figure 5. (*Continued.*)

This feature (the minimum) is controlled by the existence of slow-velocity layer in the upper 5 km of the basin, as we discuss in a later section.

3.2 Geographic pattern in Rayleigh-wave ellipticity

Rayleigh-wave ellipticity measurements at four frequencies 0.15, 0.20, 0.25 and 0.30 Hz for 50 stations are shown by colours in Fig. 7. The scale is given on the right-hand side.

A systematic geographic feature for the Rayleigh-wave ellipticity is seen most clearly in the 0.15 Hz map. The region of thick sedimentary layer, that is, the Los Angeles basin, matches well with the region dominated by orange and yellow circles (stations). Fig. 7 also shows the transition in higher-frequency maps from 0.20 to 0.30 Hz, as the basin characteristics weaken and disappear in higher-frequency bands.

Rayleigh-wave ellipticity is a function of local structure beneath each station, with some influences arising from the adjacent region due to finite horizontal wavelength of Rayleigh waves. The horizontal wavelengths vary from about 20 km at 0.15 Hz to half of it at 0.30 Hz. In order to create maps for the Rayleigh-wave ellipticity, we applied an interpolation scheme with the averaging length 20 km and created the maps in Fig. 8. The striking feature of the basin (small ellipticity in orange and yellow) is still seen in the map for 0.15 Hz.

Fig. 9 shows the same result for 0.15 Hz in Fig. 8 in a 3-D plot. It clearly depicts that the low ellipticity values are associated with the deep sedimentary region in the Los Angeles basin. Green lines are the known active faults. The fault running in the middle of the red region (Los Angeles basin) is the Newport-Inglewood Fault (NIF).

3.3 Differences in *S*-wave velocity structure inside and outside the basin

In Figs 6(a) and (b), we discussed the characteristic feature of the basin related to the minimums in the frequency versus Rayleigh wave ellipticity plot. In order to understand the cause of this minimum with respect to the inverted *S*-wave velocity structure, we solved for the *S*-wave velocity structure beneath eight stations in Figs 6(a) and (b). In Fig. 10, we compare the derived *S*-wave velocity models. The *S*-wave velocity profiles in the basin are shown by

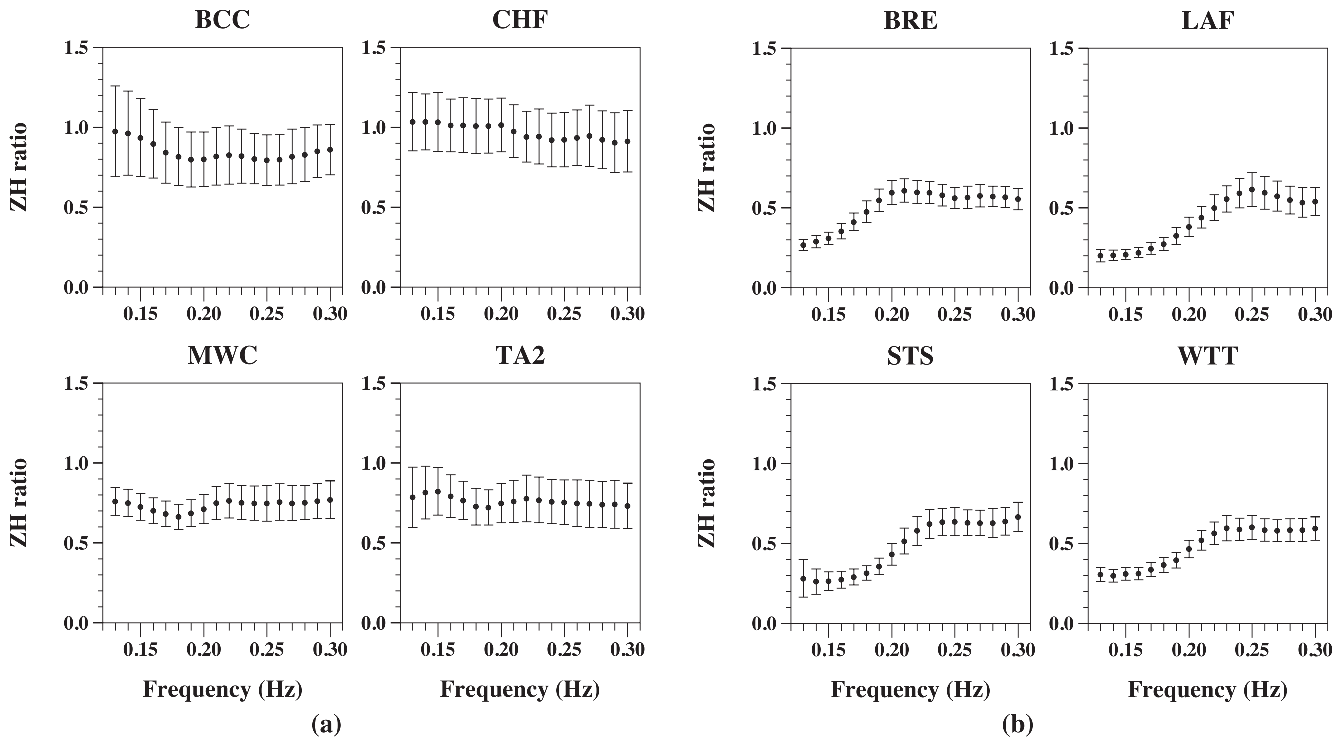

Figure 6. (a) Measured Rayleigh-wave ellipticity at four stations outside the Los Angeles basin. Frequency range is from 0.13 to 0.30 Hz. (b) Same with Fig. 5(a) except that they are at four stations in the Los Angeles basin. They have the minimum around 0.13–0.16 Hz.

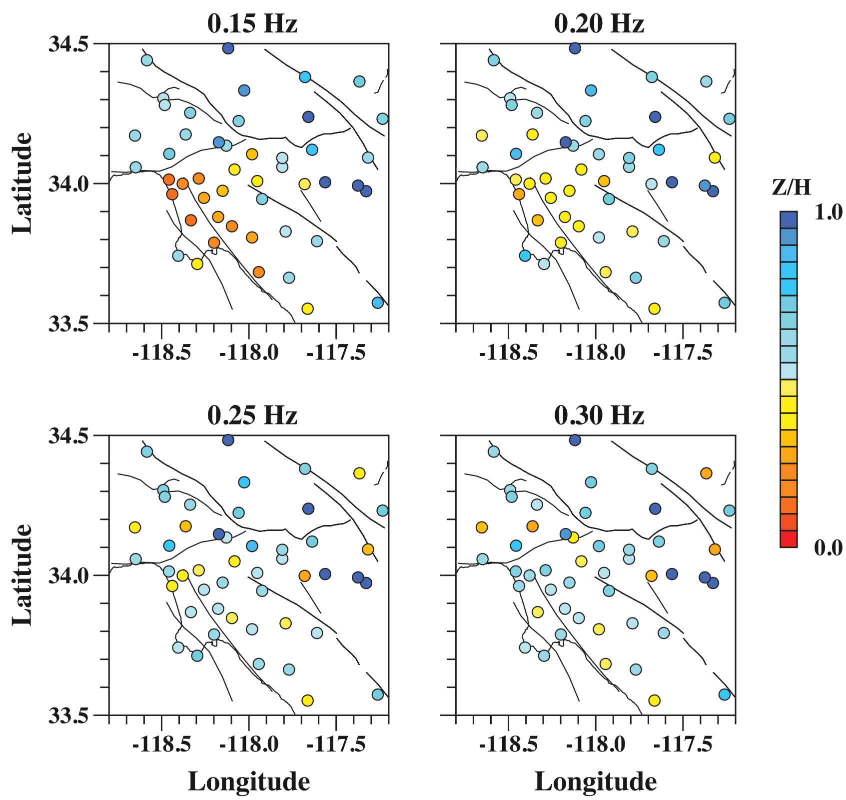

Figure 7. Rayleigh-wave ellipticity at four frequencies. Scale is given at right.

red lines (stations BRE, LAF, STS and WTT) and those outside the basin are shown by blue lines (BCC, CHF, MWC and TA2).

The *S*-wave velocity structures in Fig. 10 show very complex variations with depth both for the red and blue profiles. Many complexities in these profiles are inherited from the starting model (SCEC CVM 6.2). However, there are also clear and characteristic differences in the shallow depth ranges. Fig. 10 shows that the differences mainly exist in the upper 5.0 km with clearer differences

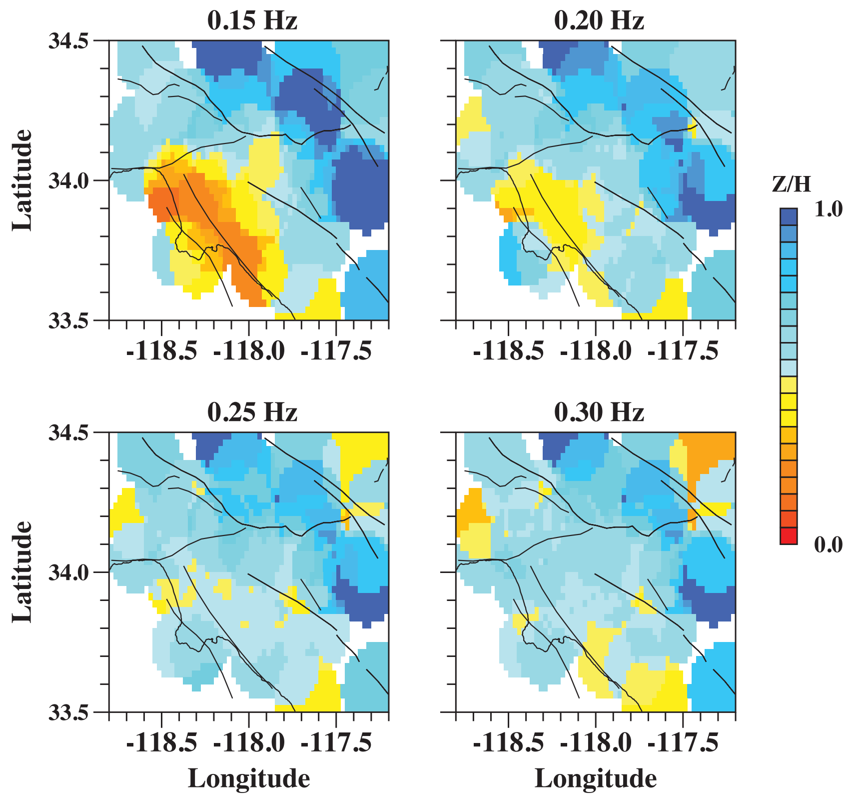

Figure 8. Rayleigh-wave ellipticity values in Fig. 7 were used to interpolate the values for the region. The horizontal wavelength of Rayleigh waves of 20 km (at 0.15 Hz) was used for interpolation. White regions indicate that there are no Rayleigh-wave ellipticity values available.

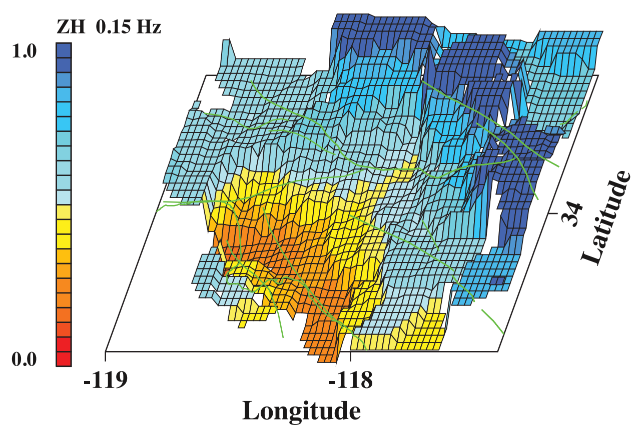

Figure 9. The 3-D view of the Rayleigh-wave ellipticity data at 0.15 Hz. The Los Angeles basin emerges through this parameter.

in the upper 3 km. Roughly speaking, *S*-wave velocities outside the Los Angeles basin (blue) are faster by about 1.0 km s^{-1} than those in the basin (red) for this shallow depth range.

Depth sensitivity kernels for *S* waves, K_β, are shown in Fig. 11. They were computed for the final models of inversion for each case. The left panel shows the *S*-wave kernels for structure at CHF, a station outside the basin. The six curves are the kernels for different frequencies from 0.10 to 0.20 Hz at an interval of 0.02 Hz. Note that they have sharp peaks in the upper 2 km of the crust with broad negative swings for depths below (2–7 km approximately).

The right panel in Fig. 11 shows the *S*-wave kernels for the same frequency range for the structure at LAF, a station in the basin. In this case, shallow kernel peaks have broader depth ranges and also have very large amplitudes. Note that there is a difference of almost a factor of 10 in amplitudes between the left panel (hard rock site) and the right panel (basin site).

These kernels clearly support that the Rayleigh-wave ellipticity data constrain *S*-wave velocity in the upper 5 km of the crust. Near the minimum of the Rayleigh-wave ellipticity (about 0.15 Hz), the kernels indicate that the data are sensitive to the upper 3 km of the crust. Thus, it seems natural to expect the inverted *S*-wave velocity results in Fig. 10, which shows the main differences in the upper 3–5 km.

3.4 Geographic patterns in *S*-wave velocity results

We divided the region of this study (Fig. 1) into 2.0 × 2.0 km blocks, derived the Rayleigh-wave ellipticity as a function of frequency for each block (by interpolation), and performed inversion for the *S*-wave velocity structure. The inversion process (such as parameterization) is basically the same as the procedure used to obtain results in Figs 5(a) and (b) except for the difference in the lowest frequency 0.13 Hz.

The *S*-wave velocity structures were parameterized for every 0.1 km in depth. Depth resolution is controlled by the finite-frequency effects, as contained in depth sensitivity kernels as in Fig. 4. A typical averaging depth (resolution) was about a few kilometres.

In order to understand the large-scale characteristics in the *S*-wave velocity variations, we computed the average *S*-wave velocity changes for two depth intervals, 0–5 and 5–10 km. The starting models, averaged over the two depth intervals, are shown in the top panels of Figs 12(a) and (b). The perturbations to *S*-wave velocity structure are shown in the bottom panels. Note that some locations show perturbations in *S*-wave velocities as large as 50 per cent.

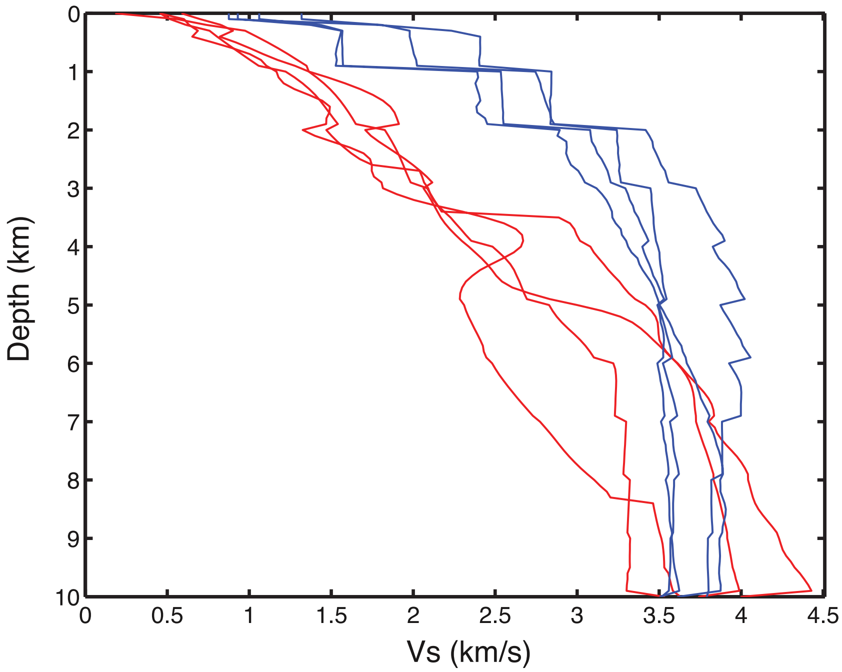

Figure 10. *S*-wave velocity depth profiles at four stations in the Los Angeles basin (red) and those at four stations outside the basin (blue). They are the stations in Figs 5(a) and (b). The minimum in the Rayelgih-wave ellipticity is related to the shallow low velocities, mostly in the upper 3–5 km.

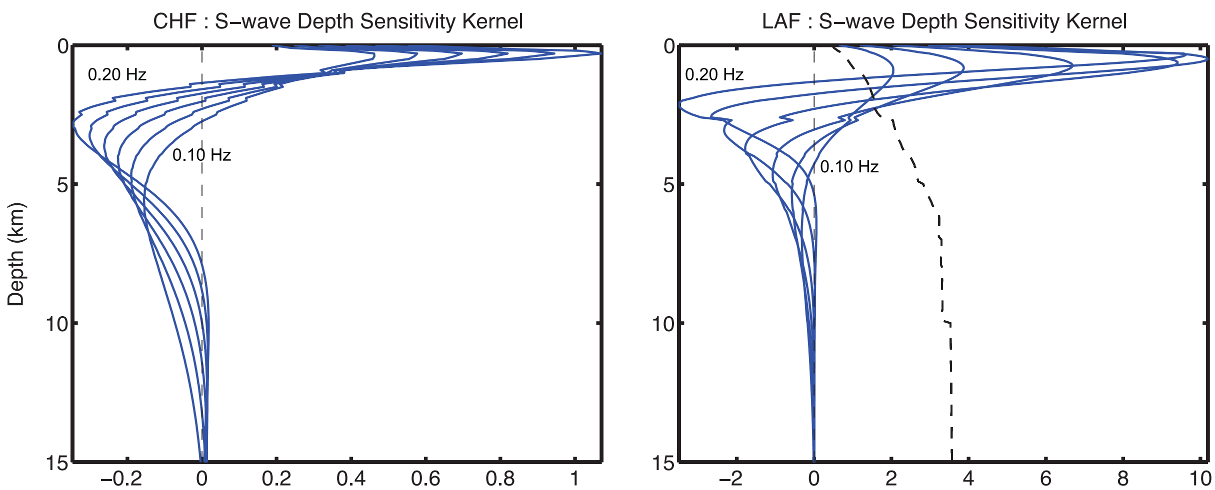

Figure 11. Depth sensitivity kernels for *S* waves at two sites, CHF (left) and LAF (right). CHF is outside the basin structure, while LAF is in the Los Angeles basin. The inverted final models for each location are used for these computations. Six profiles are for different frequencies between 0.10 and 0.20 Hz at an interval of 0.02 Hz. The lower the frequencies, the deeper the penetration of kernels. There is almost a factor of 10 difference in kernel amplitudes between left and right panels.

Gaps in the lower panels are the locations with low variance reduction. The blocks whose inversion led to less than 80 per cent variance reduction are not plotted in this figure.

For the upper 5.0 km (Fig. 12a), there are three features in the perturbed velocity structure (bottom) that are notable: (1) the eastern edge of the basin close to the northern end of the Elsinore Fault (EF), (2) along the Santa-Monica Fault (SMoF) and (3) the west side of the Palos Verdes fault (PVF). Four faults (PVF, NIF, SMoF and EF) are indicated in Figs 12(a) and (b) in the top panels.

For the eastern edge of the basin, an elongated region with large positive *S*-wave velocity variations (blue) emerged along the eastern edge of the Los Angeles basin region (Fig. 12a, bottom). The location is along the longitude 242.2° (117.8° west). The Los Angeles region can be recognized by red (orange) area in the top panel. The emergence of this pattern suggests that velocity change at the eastern edge of the basin should be much sharper than the starting model (CVM-H 6.2).

For the feature near the SMoF, there is an east–west trending narrow region (in orange and yellow), extending from the longitude 241.2° to 241.7° mainly along the north side of this fault (its approximate latitude 34.1°). This is close to the green/yellow east–west trending region in the starting model in the top panel. This narrow region separates the low-velocity region in the Los Angeles basin (south) from the low-velocity region in the San Fernando basin (north). This result indicates that velocity in the narrow (east–west) region in the starting model must be decreased, thereby reducing the

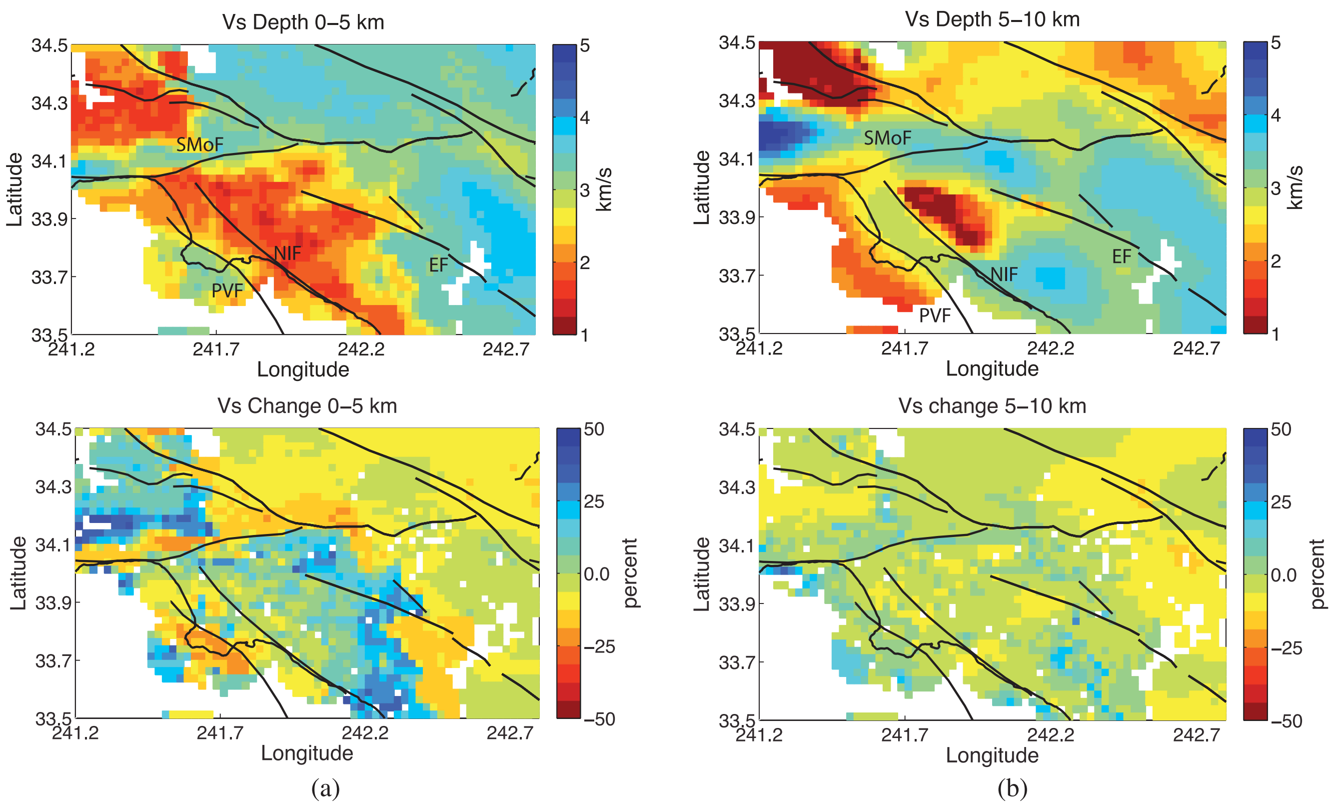

Figure 12. (a) (Top) The averaged *S*-wave starting structure in the upper 5.0 km. Four faults are indicated by SMoF, PVF, NIF and EF. Slow-velocity (red) anomaly north of SMoF contains the San Fernando basin, and slow-velocity anomaly south of SMoF is the Los Angeles basin. (Bottom) Required changes to the starting model in order to fit the Rayleigh-wave ellipticity data. White regions indicate that the variance reductions were less than 80 per cent. (b) (Top) The average *S*-wave starting structure in the depth range 5.0–10 km. (Bottom) The inverted *S*-wave perturbations for the same depth range. Data from the frequency range 0.1–0.3 Hz are clearly much less sensitive to this depth range than the upper 5 km.

contrast between this narrow region and the basins to the north side and to the south side. The existence of a narrow east–west trending region that separates the two basins is supported, however.

For the features on the west side of the PVF, our results indicate the existence of slow *S*-wave velocity regions to the west side of PVF. The starting model has fast *S*-wave velocity (CVM-H 6.2), but the results indicate that this needs to be reduced by almost 20 per cent in order to fit the Rayleigh-wave ellipticity data.

The results for the depth range between 5.0 and 10.0 km comparatively show much smaller perturbations (Fig. 12b) than the results in the upper 5.0 km (Fig. 12a). This may be expected from the kernels in Fig. 11, as they are more sensitive to the lower frequency end of kernels in our data set. Our data (Rayleigh-wave ellipticity between 0.13 and 0.30 Hz) are clearly much more sensitive to *S*-wave structures in the upper 5 km than the depths 5–10 km.

4 CONCLUSION

In order to construct a reliable shallow crustal structure, we analysed the Rayleigh-wave ellipticity data derived from seismic noise below 0.3 Hz. We developed an approach for Rayleigh-wave ellipticity that reduces the effects from Love waves and *S* waves.

The effects of removal of *S* waves and Love waves in the horizontal components changed the estimates of Rayleigh-wave ellipticity by about 20 per cent. From this result, we inferred that the Love-wave energy (and *S* waves) in seismic noise about 0.15 Hz is about 50 per cent of the Rayleigh-wave energy. Inversion of this revised estimates for Rayleigh-wave ellipticity yielded an *S*-wave velocity structure that was different about 20 per cent. If we accept this value, the bias caused by body waves and Love waves on this method (the *H*/*V* type method) may be about this order. We have obtained this result for a low-frequency range, 0.1–0.3 Hz; thus, the level of bias may be quite different for high-frequency ranges.

We showed that the Rayleigh-wave ellipticity has a specific frequency-dependent feature in the LA basin, specifically the minimum near 0.13–0.16 Hz. This feature disappears towards 0.30 Hz. By inverting this Rayleigh-wave ellipticity data, we derived a model that improved the reference seismic model in the region (SCEC CVM-H 6.2). The main contribution of this approach is the improvement in the upper 5 km of the crust, which may be crucial for predicting ground motions in the long-period range (period about 5–10 s). In the derived *S*-wave velocity models, we found that (1) the eastern edge of the Los Angeles basin has sharper velocity transition, (2) a faster velocity east–west stripe is required just north of the SMoF but not as fast as the reference model indicates and (3) slower velocity is needed on the west side of the PVF.

This method is applicable to any region of the world as long as there is a good network of seismometers that record seismic noise. It may be a useful approach for accurately determining the average *S*-wave velocity structure in the upper 5–10 km of the crust.

ACKNOWLEDGMENTS

We thank Dr. Stefano Parolai for his extensive review. This study benefited greatly from efficient service by the SCEC data centre. This research was supported by the Southern California Earthquake

Center and NSF-EAR0408742. SCEC is funded by NSF Cooperative Agreement EAR-0106924 and USGS Cooperative Agreement 02HQAG0008.

REFERENCES

Aki, K., 1957. Space and time spectra of stationary stochastic waves, with special reference to microtremors, *Bull. Earthq. Res. Inst.,* **35,** 415–456.

Arai, H. & Tokimatsu, K., 2004. S-wave velocity profiling by inversion of microtremor H/V spectrum, *Bull. seism. Soc. Am.,* **94,** 53–63.

Asten, M.W. & Boore, D., 2005. Comparison of shear-velocity profiles of unconsolidated sediments near the Coyote borehole (CCOC) measured with fourteen invasive and non-invasive methods, Blind comparisons of shear-wave velocities at closely-spaced sites in San Jose, California, Asten and Boore (Editors), *U.S. Geological Survey Open-File report 2005–1169,* part 1, 35pp. (http://pubs.usgs.gov/of/2005/1169/).

Bard, P.-Y., 1998. Microtremor measurements: a tool for site effect estimation?, in *Proceedings of the 2nd Int. Symp. Effects of Surface Geology on Seismic Motion,* Yokohama, Balkema, Vol. 3, pp. 1251–1279.

Bonnefoy-Claudet, S., Cotton, F. & Bard, P.-Y., 2006. The nature of the seismic noise wave field and its implication for site effects studies: a literature review, *Earth Sci. Rev.,* **79,** 205–227.

Bonnefoy-Claudet, S., Kohler, A., Cornou, C., Wathelet, M. & Bard, P.-Y., 2008. Effects of Love waves on microtremor H/V method, *Bull. seism. Soc. Am.,* **98,** 288–300.

Boore, D.M., 2006. Determining subsurface shear-wave velocities: a review, in *Proceedings of the 3rd Int. Symp. Effects of Surface Geology on Seismic Motion,* Grenoble, France, p. 103.

Campillo, M. & Paul, A., 2003. Long-range correlations in the seismic coda, *Science,* **299,** 547–549.

Capon, J., 1972. Long-period signal processing results for LASA, NORSAR and ALPA, *Geophys. J. R. astr. Soc.,* **31,** 279–296.

Cessaro, R.K., 1994. Sources of primary and secondary microseisms, *Bull. seism. Soc. Am.,* **84,** 142–148.

Chen, P., Zhao, L. & Jordan, T.H., 2007. Full 3D tomography for the crustal structure of the Los Angeles region, *Bull. seism. Soc. Am.,* **97**(4), 1094–1120.

Fäh, D., Kind, F. & Giardini, D., 2001. A theoretical investigation of average H/V ratios, *Geophys. J. Int.,* **145,** 535–549.

Field, E. & Jacob, K., 1993. The theoretical response of sedimentary layers to ambient seismic noise, *Geophys. Res. Lett.,* **20,** 2925–2928.

Friedrich, A., Krüger, F. & Klinge, K., 1998. Ocean-generated microseismic noise located with the Grafenberg array, *J. Seismol.,* **2,** 47–64.

Hauksson, E., 2000. Crustal structure and seismicity distribution adjacent to the Pacific and north America plate boundary in southern California, *J. geophys. Res.,* **105,** 13 875–13 903.

Horike, M., 1985, Inversion of phase-velocity of long-period microtremors to the S-wave-velocity structure down to the basement in urbanized areas, *J. Phys. Earth,* **33**(2), 59–96.

Kawase, H., Satoh, T., Iwata, T. & Irikura, K., 1998. S-wave velocity structure in the San Fernando and Santa Monica areas, in *Effects of Surface Geology on Seismic Motion,* pp. 733–740, eds Irikura, K., Kudo, K., Okada, H. & Sasatani, T., Balkema, Rotterdam.

Kohler, M., Magistrale, H. & Clayton, R.W., 2003. Mantle heterogeneities and the SCEC reference three-dimensional seismic velocity model version 3, *Bull. seism. Soc. Am.,* **93,** 757–774.

Konno, K. & Ohmachi, T., 1998. Gorund-motion characteristics estimated from spectral ratio between horizontal and vertical components of microtremor, *Bull. seism. Soc. Am.,* **88,** 228–241.

Kudo, K., 1995. Practical estimates of site response, in *Proceedings of the 5th Int. Conf. Seismic Zonation,* Nice, France.

Lachet, C. & Bard, P.-Y., 1994. Numerical and theoretical investigations on the possibilities and limitations of Nakamura's technique, *J. Phys. Earth,* **42,** 377–397.

Lermo, J. & Chavez-Garcia, F.J., 1994. Are microtremors useful in site response evaluation? *Bull. seism. Soc. Am.,* **84,** 1350–1364.

Liu, H.-P., Boore, D., Joyner, W., Oppenheimer, D., Warrick, R., Xhang, W., Hamilton, J. & Brown, L., 2000. Comparison of phase velocities from array measurement sof Rayleigh waves associated with microtremor and results calculated from borehole shear-wave velocity profiles, *Bull. seism. Soc. Am.,* **90,** 666–678.

Longuet-Higgins, M.S., 1950. A theory of the origin of microseisms, *Philos. Trans. R. Soc. Lond., A,* **243,** 1–35.

Lunedei, E. & Albarello, D., 2010. Theoretical HVSR curves from full wavefield modelling of ambient vibrations in a weakly dissipative layered earth, *Geophys. J. Int.,* **181,** 1093–1108.

Nakamura, Y., 1989. A method for dynamic characteristics estimation of subsurface using microtremor on the ground surface, *Q. Rep. Railway Tech. Res. Inst.,* **30**(1), 25–33.

Nishida, K., Kawakatsu, H. & Obara, K., 2008. Three-dimensional crustal S wave velocity structure in Japan using microseismic data recorded by Hi-net tiltmeters, *J. geophys. Res.,* **113,** B10302, doi:10.1029/2007JB005395.

Nogoshi, M. & Igarashi, T., 1971. On the amplitude characteristics of microtremor (part 2), *J. seism. Soc. Japan,* **24,** 26–40 (in Japanese with English abstract).

Okada, H., 2003. *The Microtremor Survey Method,* in Geophysical Monograph Series, Number 12, Society of Exploration Geophysicists, Tulsa.

Parolai, S., Picozzi, M., Richwalski, S.M. & Milkereit, C., 2005. Joint inversion of phase velocity dispersion and H/V ratio curves from seismic noise recordings using a genetic algorithm, considering higher modes. *Geophys. Res. Lett.,* **32,** L01303, doi:10.1029/2004GL021115.

Parolai, S., Richwalski, S.M., Milkereit, C. & Fäh, D., 2006. S-wave velocity profiles for earthquake engineering purposes for the Cologne area (Germany), *Bull. Earthq. Eng.,* **4,** 65–94.

Plesch, A., Tape, C. & Shaw, J.H. members of the USR working group, 2009. CVM-H 6.0: inversion integration, the San Joaquin Valley and other advances in the community velocity model, in *2009 Southern California Earthquake Center Annual Meeting, Proceedings and Abstracts,* vol. 19, pp. 260–261.

Prindle, K. & Tanimoto, T., 2006. Teleseismic surface wave study for S-wave velocity structure under an array: Southern California, *Geophys. J. Int.,* **166,** 601–621.

Saito, T., 2010. Love-wave excitation due to the interaction between a propagating ocean wave and the sea-bottom topography, *Geophys. J. Int.,* **182,** 1515–1523.

Sanchez-Sesma, F.J. *et al.*, 2011. A theory for microtremor H/V spectral ratio: application for a layered medium, *Geophys. J. Int.,* **186,** 221–225.

Scherbaum, F., Hinzen, K.-G. & Ohrnberger, M., 2003. Determination of shallow shear wave velocity profiles in the Cologna, Germany area using ambient vibrations, *Gephys. J. Int.,* **152,** 597–612.

Schulte-Pelkum, V., Earle, P.S. & Vernon, F.L., 2004. Strong directivity of ocean-generated seismic noise, *Geochem. Geophys. Geosyst.,* **5**(3), doi:10.1029/2003GC000520.

Shapiro, N.M., Campillo, M., Stehly, L. & Ritzwoller, M., 2005. High-resolution surface-wave tomography from ambient seismic noise, *Science,* **307,** 1615–1618.

Süss, M.P. & Shaw, J.H., 2003. P-wave seismic velocity structure derived from sonic logs and industry reflection data in the Los Angeles basin, California, *J. geophys. Res.,* **108**(B3), B2170, doi: 10.1029/2001JB001628.

Tanimoto, T. & Alvizuri, C., 2006. Inversion of the HZ ratio of microseisms for S-wave velocity in the crust, *Geophys. J. Int.,* **165,** 323–335.

Tanimoto, T. & Rivera, L., 2005. Prograde Rayleigh wave particle motion, *Geophys. J. Int.,* **162,** 399–405.

Tanimoto, T. & Tsuboi, S., 2009. Variational principle for Rayleigh wave ellipticity *Geophys. J. Int.,* **179,** 1658–1668.

Tanimoto, T., Ishimaru, S. & Alvizuri, C., 2006. Seasonality in particle motion of microseisms, *Geophys. J. Int.,* **166**(1), 253–266.

Tape, C., Liu, Q., Maggi, A. & Tromp, J., 2009. Adjoint tomography of the southern California crust, *Science,* **325**(5943), 988–992.

Tape, C., Liu, Q., Maggi, A. & Tromp, J., 2010. Seismic tomography of the southern California crust based on spectral-element and adjoint methods, *Geophys. J. Int.,* **180**(1), 433–462.

Tokimatsu, K., 1997. Geotechnical site characterization using surface waves, in *Earthquake Geotechnical Engineering,* pp. 1333–1368, ed. Ishihara, K., Balkema, Rotterdam.

Yamanaka, H. & Ishida, H., 1996. Application of genetic algorithm to an inversion of surface-wave dispersion data, *Bull. seism. Soc. Am.,* **86,** 436–444.

Yamanaka, H., Takemura, M., Ishida, H. & Niwa, M., 1994. Characteristics of long-period microtremors and their applicability in exploration of deep sedimentary layers, *Bull. seism. Soc. Am.,* **84**(6), 1831–1841.

Yano, T., Tanimoto, T. & Rivera, L., 2009. The ZH ratio method for long-period seismic data: inversion for S-wave velocity structure, *Geophys. J. Int.,* **179,** 413–424.